CHALMERS
UNIVERSITY OF TECHNOLOGY

Evaluation of wind tunnel interference on numerical prediction of wheel aerodynamics

Journal of Wind Engineering & Industrial Aerodynamics 224 (2022) 104945

Contents lists available at ScienceDirect

Journal of Wind Engineering & Industrial Aerodynamics

journal homepage: www.elsevier.com/locate/jweia

Evaluation of wind tunnel interference on numerical prediction of wheel aerodynamics

Erik Josefsson [a,*], Teddy Hobeika [b], Simone Sebben [a]

[a] Department of Mechanics and Maritime Sciences, Chalmers University of Technology, 412 96 Gothenburg, Sweden
[b] Aerodynamics, Volvo Cars, 418 78 Gothenburg, Sweden

ARTICLE INFO

Keywords:
Vehicle aerodynamics
Wheels
Tyres
Drag
CFD
Wind tunnel

ABSTRACT

For a passenger vehicle, approximately 25% of the total aerodynamic drag originates from the wheels, making the aerodynamics of wheels a significant factor for the overall performance of a vehicle. To understand the complex flow field created by the rotational condition and geometry of these bluff-bodies, numerical simulations are often used. However, computations are frequently performed in domains that replicate open road conditions, differing from the conditions of wind tunnels. Therefore, to properly validate a CFD procedure and to correlate physical tests to numerical results, interference effects of the wind tunnel need to be investigated and their impact on the aerodynamics of wheels analysed and compared to that of open road calculations.

In this study, numerical simulations on the DrivAer model were performed using different tyres and rims in both open road conditions and with the inclusion of a detailed model of a slotted walls wind tunnel. The results of the simulations are compared to experimental data, consisting of forces and flow field measurements. It was found that the inclusion of the wind tunnel in the computations improves the prediction of the flow fields, resulting in better prediction of both the absolute drag values and the drag deltas between configurations.

1. Introduction

To meet new legislation and customer expectations of reduced CO_2 emissions or extended vehicle driving range, OEMs strive to improve the energy efficiency of their fleets. At velocities above approximately 80 km/h the aerodynamic drag is the largest resisting force acting on a passenger vehicle (Hucho, 1998). It is well acknowledged that the wheels can contribute to 25% or more of a vehicle's total drag (Wickern et al., 1997; Cogotti, 1983), making them an influential factor to consider when reducing the overall aerodynamic resistance. The rotation, detailing and bluff-body shape of the wheels result in a complex flow that is challenging to understand and simulate. Still, Computational Fluid Dynamics (CFD) is often used, alone or as a complement to experiments, as it can provide more insight around these regions. However, such simulations are usually performed in virtual domains that replicate open road conditions, where a large computational box with negligible blockage is used along with a fully moving ground plane. Although this is more representative of what happens on the road, it differs from the conditions of wind tunnel tests, which are used for vehicle development, certification and validation of numerical models. Additionally, wind tunnels remain an essential tool for vehicle manufacturers where results from new designs can be obtained within minutes compared to numerical simulations requiring hours, or even days, for each new design. Hence, it is important to comprehend how the interference from the wind tunnel geometry and its moving ground system affect the flow around the wheels, thus allowing for an improved correlation between the two tools.

In the past, multiple studies on the flow around wheels have considered a simplified isolated wheel (Croner et al., 2013; Schnepf et al., 2015; Reiß et al., 2020; Diasinos et al., 2015). Although these works gave good insight into the complexity of the phenomena, they lacked the effects related to the encapsulation of the wheels within the wheelhouses. For wheels integrated with a passenger vehicle, many studies have focused on the difference between stationary and rotating boundary conditions (Wang et al., 2019, 2020; Wickern et al., 1997; Wäschle, 2007). Wickern et al. (1997) showed the importance of wheel rotation and that the rotation has a considerable impact on the drag. This was further established by Wäschle (2007), who also compared stationary and rotating wheels, identifying the dominant flow features for both cases. Other investigations have demonstrated the significance of considering both the rim and the tyre. For example, Mayer and Wiedemann (2007) identified differences of approximately $\Delta C_D = 0.020$ between

* Corresponding author.
E-mail addresses: erik.josefsson@chalmers.se (E. Josefsson), teddy.hobeika@volvocars.com (T. Hobeika), simone.sebben@chalmers.se (S. Sebben).

https://doi.org/10.1016/j.jweia.2022.104945
Received 14 October 2021; Received in revised form 4 February 2022; Accepted 18 February 2022
Available online 15 March 2022

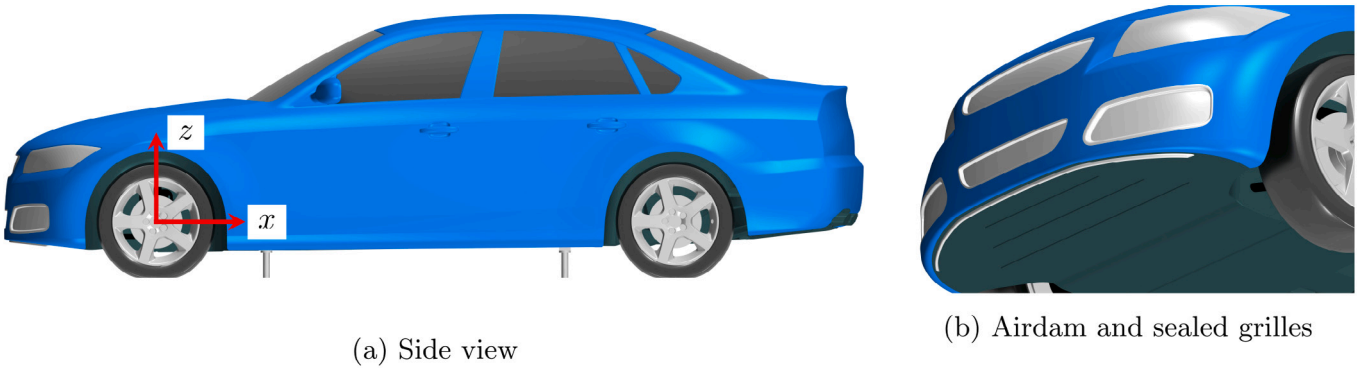

(a) Side view (b) Airdam and sealed grilles

Fig. 1. DrivAer geometry used in the study.

(a) Slick (S) (b) Rain (R) (c) Lateral (L) (d) Detailed (D)

Fig. 2. Tyre patterns investigated.

various rims and Wittmeier et al. (2014) found that the drag was greatly influenced by the tyre profile, especially at the outer shoulder.

Hobeika and Sebben (2018a) looked at the effect of tyre patterns on the drag of a full-scale car using both wind tunnel tests and numerical simulations. They found that the effect of adding rain grooves on a slick tyre was well replicated in the numerical simulations, whereas the addition of lateral grooves was not as well predicted, especially for the closed rim. In a study involving several rim designs, Koitrand et al. (2015) also identified that the simulations could not accurately replicate the wind tunnel results of a fully closed rim. Both works were performed using open road simulation conditions. Hobeika and Sebben (2018a) theorised that part of the difference between the experiments and the numerical results were due to interference effects of the wind tunnel, which were not accounted for in the simulations. Fischer et al. (2008, 2010) included the geometry of an open jet wind tunnel in simulations of a notchback scale model and found that the flow predictions generally improved. Comparing different underbody configurations, Cyr et al. (2011) also found that the inclusion of the wind tunnel resulted in better agreement to experiments. Ljungskog et al. (2019) modelled a slotted wall wind tunnel and obtained a better prediction of absolute drag values compared to open road simulations. However, the delta coefficients among configurations did not always improve. According to Ljungskog et al. (2019), the largest discrepancies between the two domains occurred in areas of strong acceleration, such as around the wheels and between open and closed rims.

Few studies have focused on the effect of adding the wind tunnel geometry in numerical simulations on the ability to predict wheel flows. Haag et al. (2017) investigated a variety of rims for a scale model of the DrivAer in an open jet wind tunnel with fully moving ground. The wheels were supported by struts and were disconnected from the vehicle body. Comparing experiments and numerical simulations, where parts of the wind tunnel geometry were included, they observed that the differences between the rims could be well predicted. No comparisons to open road simulations were performed, however, a large influence from including the wheel struts was noted. The present work aims at investigating the influence of including the wind tunnel geometry and its ground simulation system on the accuracy of numerical simulations using a full-scale model of the DrivAer. The focus of the work is on the capability of the CFD method to predict changes in drag for various tyre and rim combinations. The results of the computations are compared to physical measurements from the wind tunnel.

2. Methodology

2.1. Vehicle geometry

The test object is a version of the DrivAer reference model, which has been extensively studied for example in Heft et al. (2012), Wittmeier and Kuthada (2015), Hupertz et al. (2018), Ekman et al. (2020), Avadiar et al. (2018) and Strangfeld et al. (2013). The DrivAer was initially introduced by Heft et al. (2012) and has since been updated to include a detailed engine bay with cooling flow (Wittmeier and Kuthada, 2015). This study uses the open cooling DrivAer presented by Hupertz et al. (2018) which features a detailed engine bay and underbody as well as a simplified suspension system and rotating brake discs. The notchback configuration with the sealed grille and with rear-view mirrors is used, as shown in Fig. 1. The vehicle is also equipped with a small airdam (Fig. 1(b)) introduced to simplify the separation at the leading edge of the underbody, which has proven challenging to predict consistently, both in wind tunnels (Hupertz et al., 2021) and with CFD (Ashton et al., 2019). The cross-section of the airdam is roughly rectangular and measures 10×10 mm. As shown in Fig. 1(a), the rocker panel restraint posts, used for mounting the vehicle in the wind tunnel, are replicated in the CFD model with the wind tunnel included but removed for the open road simulations. The coordinate system used in this work is placed at the front axle, as shown, with the ground at $z = -317$ mm.

The tyres are a set of modified racing tyres (210/635R17) with a diameter of 640 mm and a width of 218 mm. The tyres are studied in four configurations; slicks (S), rain (R), lateral (L) and detailed (D), see Fig. 2. They are mounted on production rims which are tested in an original (open) configuration as well as a fully covered (closed) configuration, Fig. 3. The tyres were deformed to replicate the static deformation caused by the vehicle weight. Since they are stiff racing tyres the dynamic deformations are small, as described by Hobeika and Sebben (2018a).

(a) Open rim (OR) (b) Closed rim (CR)

Fig. 3. Rims used in the study.

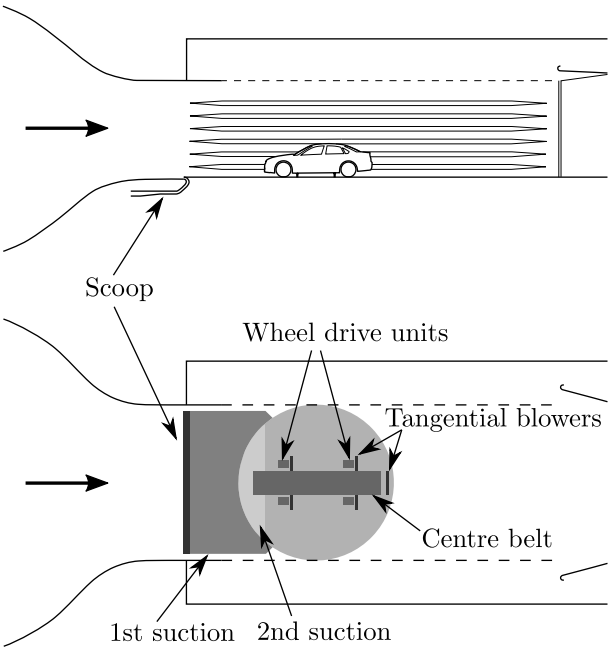

Fig. 4. Layout of the boundary layer control system in PVT.
Source: Adapted from Ljungskog et al. (2019). Drawn to scale.

2.2. Experimental setup

For the experimental investigations, the Ford Open Cooling DrivAer (Hupertz et al., 2018, 2021) was tested in the Volvo Cars Aerodynamic Wind Tunnel (PVT). The wind tunnel has a slotted wall test section and is equipped with a boundary layer control system featuring a scoop, distributed suction, a five-belt moving ground system and tangential blowers, Fig. 4. The tangential blowers were not activated to facilitate later comparison with CFD results. The wind tunnel is described in detail by Sternéus et al. (2007).

2.2.1. Blockage correction

The correction method used at PVT is described in detail by Eng and Walker (2009). Basically, the blockage corrected C_D is calculated as

$$C_{D,\text{corr}} = \frac{C_{D,\text{uncorr}} + \Delta C_{D,\text{HB}}}{\left(1+\varepsilon_s+\varepsilon_w\right)^2}, \tag{1}$$

where the dynamic pressure is corrected for solid body displacement, ε_s, and wake blockage, ε_w. These are calculated as

$$\varepsilon_s = \tau\sqrt{\frac{V}{L}}\frac{A}{A_{\text{TS}}^{3/2}} \quad \text{and} \quad \varepsilon_w = \frac{A}{A_{\text{TS}}}\left(\frac{C_{D,\text{uncorr}}}{4}+\eta\right). \tag{2}$$

Here V, A and L are the volume, frontal area and length of the vehicle and $A_{\text{TS}} = 27.1\,\text{m}^2$ is the cross sectional area of the test section. $\tau = 0.8315$ is the tunnel shape factor and $\eta = 0.41$ is an empirical wake blockage constant. The drag is also corrected for horizontal buoyancy, $\Delta C_{D,\text{HB}}$. This term considers the horizontal buoyancy both of the empty tunnel, which can be measured, and induced by the vehicle, which is based on empirical data. For the DrivAer notchback, where $V = 6.58\,\text{m}^3$, $A = 2.17\,\text{m}^2$ and $L = 4.61\,\text{m}$, and the range of C_D values considered in this work, the corrected drag is approximately $C_{D,\text{corr}} \approx 0.936 C_{D,\text{uncorr}}$.

2.2.2. Measurements

In addition to determining the forces, flow field measurements were performed using the traversing gear in the wind tunnel. Two 12-hole Omniprobes were mounted to the probe arm and measured the pressures. The velocity, the static and the total pressure could then be derived using the calibration performed by the manufacturer. The probes are reported to be accurate to within 3% in terms of velocity magnitude (corresponding to approximately 1 m/s in the freestream) and ±1.5° in terms of flow direction (Aeroprobe corporation, 2015). The measurements were taken in the yz-plane $x = 4000\,\text{mm}$, located approximately 200 mm behind the rearmost part of the car bumper.

2.3. Numerical setup

The numerical simulations are performed using Star-CCM+. The Improved Delayed Detached Eddy Simulation (IDDES) method is used and the URANS regions of the flow are modelled with the SST $k-\omega$ turbulence model. All variables are discretised in space with the hybrid second-order upwind/bounded central differencing scheme and in time with an implicit second-order scheme.

2.3.1. Computational domains

Two computational domains are adopted. For replicating open road conditions, a rectangular domain is used. The domain is $15.2l$ long, $8.7l$ wide and $6.6l$ tall, where l is the length of the vehicle. The vehicle is placed $4.3l$ downstream of the inlet and $9.9l$ upstream the outlet, as shown in Fig. 5(a). The domain size and distances from the inlet and outlet are larger than those recommended by Siemens (2021) to guarantee a correct stagnation pressure at the vehicle front and to allow the rear wake to develop. At the inlet, a uniform velocity profile of 140 km/h is prescribed along with a turbulence intensity of 0.1%, corresponding to the conditions in the physical wind tunnel. The same velocity is used on the ground, which is modelled as a moving wall, to achieve the desired relative velocity between the vehicle and the ground. The outlet is modelled as a pressure outlet with a gauge pressure of 0 Pa. For the sides and top of the domain a zero gradient condition is used.

For the simulations including the wind tunnel geometry, a detailed model of PVT is used. The virtual model is the same as described by Ljungskog et al. (2019) and consists of the high-speed leg of the wind tunnel, starting at the settling chamber and contraction, through the test section and diffuser, Fig. 5(b). A mass flow inlet in the settling chamber is used in combination with a pressure outlet placed at the end of an extension of the diffuser. The inlet mass flow is tuned to result in a velocity of 140 km/h using the same method as in the physical wind tunnel. Measuring the pressure drop over the nozzle, ΔP, the reference velocity is calculated as

$$U_\infty = \sqrt{\frac{2k_q\Delta P}{\rho}}, \tag{3}$$

where k_q is a calibration constant from the commissioning of the wind tunnel and ρ is the air density. The turbulence intensity is 0.1%, as in the physical tunnel. The reference pressure can be calculated as

$$P_\infty = P_{C2} + k_p\Delta P, \tag{4}$$

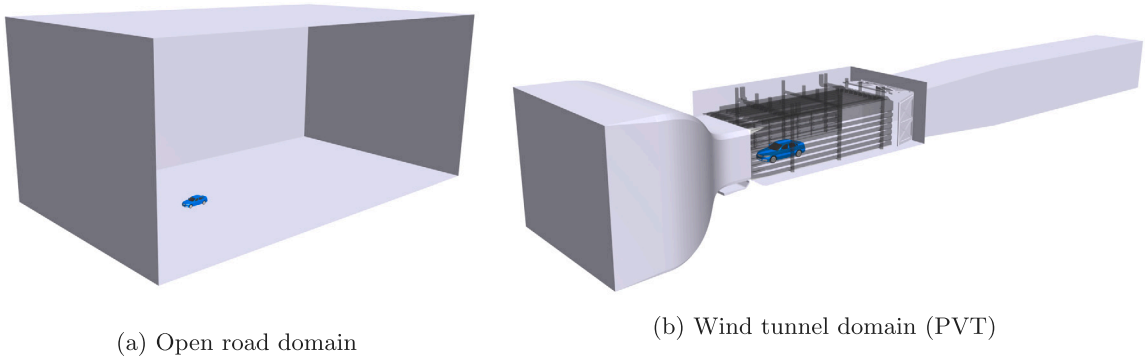

Fig. 5. The computational domains representing open road and wind tunnel conditions. The domains are not shown in the same scale.

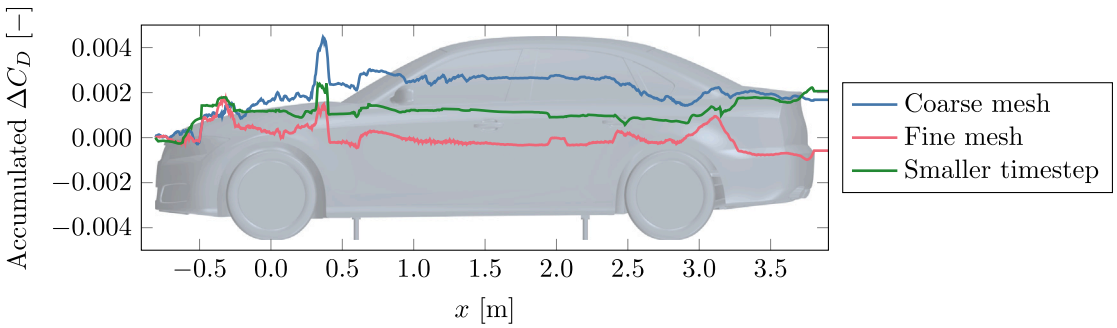

Fig. 6. Accumulated ΔC_D for different meshes and time steps. (For interpretation of the references to colour in this figure legend, the reader is referred to the web version of this article.)

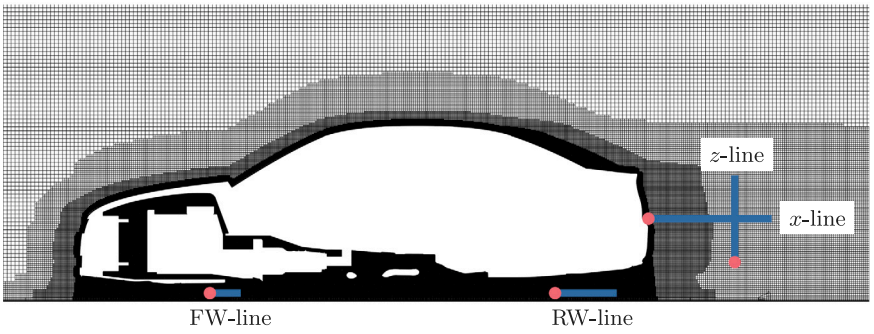

Fig. 7. Mesh at the vehicle centreline ($y = 0$) along with the lines used for the two-point correlation. The red markers indicate the start of the sampling lines. (For interpretation of the references to colour in this figure legend, the reader is referred to the web version of this article.)

where P_{C2} is the pressure measured at the nozzle exit and k_p is another calibration coefficient. This is needed in the numerical simulations since the outlet, where zero gauge pressure is prescribed, is placed downstream of the diffuser, resulting in a test section reference pressure below zero. For the simulations with the wind tunnel geometry, these expressions are used for the non-dimensionalisation of forces and pressures. For the open road simulations, the reference velocity is taken as the inlet velocity (140 km/h) and the reference pressure as the outlet pressure (0 Pa).

The full boundary layer control system is modelled using the approach described by Ljungskog et al. (2019) except for the tangential blowers as they were not used during the physical wind tunnel campaign.

2.3.2. Mesh study

A hexahedral dominant mesh is used with prism layers on all no-slip walls. For the external surfaces a cell size between 1 and 4 mm is used along with 12 prism layers. The prism layers have a total height of

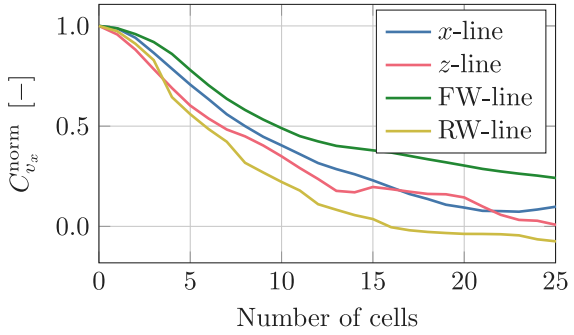

Fig. 8. Two-point correlation for the streamwise velocity along the lines illustrated in Fig. 7.

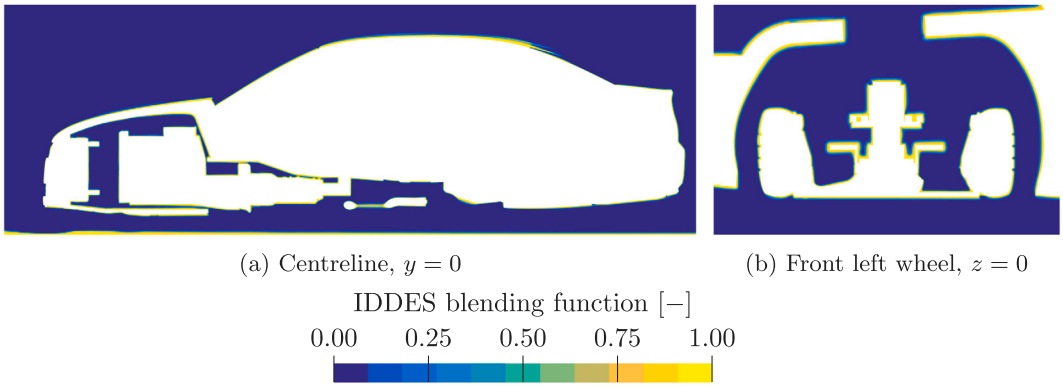

Fig. 9. IDDES blending function, indicating regions of LES (zero) and URANS (one).

10 mm with a first cell height of 0.015 mm, resulting in a growth rate of 1.7 and $y^+ < 1$. At the wheels, additional refinements are used with a surface size of 1 to 2 mm. For the simulations including the wind tunnel geometry, a high y^+ approach ($30 < y^+ < 150$) is used for the wind tunnel walls. The mesh strategy follows the recommendations by Hobeika and Sebben (2018b) and Ljungskog et al. (2019).

The mesh sensitivity is investigated by both refining and coarsening the mesh. The mesh study is performed using the wind tunnel domain since this mesh is more complex to build and, therefore, judged to be the more challenging. The results are presented for the rain grooved tyre with the closed rim, although similar investigations were also performed for other wheel configurations. A baseline mesh, consisting of 223 million cells, is compared to a coarser (175 million cells) and a finer mesh (294 million cells) created by coarsening and refining the entire mesh while keeping the y^+ values and the height of the prism layers constant. In Fig. 6, the accumulated drag for the coarse and fine meshes are shown in comparison to the baseline. Some differences are observed, most notably around the beginning and end of both the front and rear wheelhouses. However, these are small, particularly for the fine mesh, with a maximum deviation of 0.002 ΔC_D and an overall deviation of 0.0005 ΔC_D. Fig. 6 also includes the accumulated ΔC_D for a smaller time step than the baseline. This will be further discussed in Section 2.3.3.

Additionally, the mesh resolution is evaluated by examining the two-point correlation of the streamwise velocity, v_x, along the lines shown in Fig. 7. The two lines downstream of the vehicle are located at $y = 0$, whereas the lines under the vehicle are located at $y = 750$ mm, at the centreline of the right-hand side wheels. The two-point correlation of a variable ξ is calculated using its fluctuating component, ξ', as

$$C_{\xi}^{\text{norm}}\left(\vec{x}_A, \vec{x}_B\right) = \frac{\overline{\xi'\left(\vec{x}_A\right)\xi'\left(\vec{x}_B\right)}}{\xi'_{\text{RMS}}\left(\vec{x}_A\right)\xi'_{\text{RMS}}\left(\vec{x}_B\right)}, \qquad \xi'_{\text{RMS}}\left(\vec{x}\right) = \overline{\xi'\left(\vec{x}\right)^2}^{1/2}, \tag{5}$$

where $\vec{x}_A$ and $\vec{x}_B$ are the spatial coordinates investigated. As shown by Davidson (2009) the two-point correlation gives a better indication of the resolution of the flow, compared to the fraction of resolved turbulent kinetic energy. According to Davidson (2009) the largest eddies should be resolved by at least eight cells for coarse LES. Hence, a correlation larger than zero is sought for a separation distance of at least eight cells. As can be seen in Fig. 8, this criterion is fulfilled for all four lines.

To ensure a valid distinction between the LES and URANS regions, the IDDES blending function is considered, Fig. 9. As can be seen, away from the boundaries, LES is used and approaching the wall the blending function shields the URANS region as desired.

Altogether, the baseline mesh, as shown in Fig. 7, is considered to be sufficient and is used throughout this work. For the open road cases the same refinements are used around the car, resulting in a mesh consisting of 165 million cells.

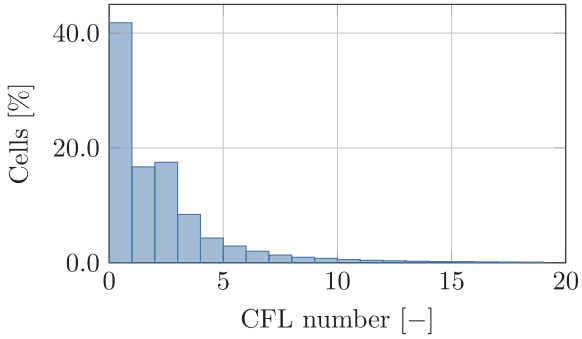

Fig. 10. Distribution of CFL number for all cells in the domain.

2.3.3. Time step and averaging time study

The simulations are initialised by steady-state RANS before switching to the unsteady IDDES method. Initially, a coarse time step is used allowing the unsteady solution to develop. The time step is then stepwise lowered until reaching the final value of 2.5×10^{-4} s. After the flow stabilises at the finest time step, the averaging is started.

The time step of 2.5×10^{-4} s is chosen to achieve a CFL number of approximately one in the majority of the domain. Although larger CFL numbers are partly obtained (Fig. 10), the time step should be sufficient as, according to Ekman et al. (2019), accurate results can be obtained for CFL numbers of 20. The cells with high CFL numbers are found in areas of high acceleration, such as around the bumper, wheels and contact patches. The validity of the time step is further investigated by performing a simulation using a finer time step, 1.25×10^{-4} s. The result is presented in Fig. 6 (green line) and shows that reducing the time step has very little influence, with a maximum deviation in the accumulated drag of only 0.002 ΔC_D.

Fig. 11 shows the instantaneous values and the running averages of C_D in the two domains. The solution is averaged for 2 s, corresponding to 17 flow passages over the vehicle, which allows a convergence of the running average to within 0.001 C_D in both computational domains.

2.3.4. Wheel modelling

The wheels are modelled using the hybrid approach Moving Reference Frame-grooves (MRFg), suggested by Hobeika and Sebben (2018a,b). In this approach, a sliding mesh (SM) is used for the rims while the tyre is modelled with a rotating wall (RW) boundary condition, except for the lateral grooves where the Moving Reference Frame (MRF) is employed. Sliding mesh is the method of choice for the motion of the rim spokes (Haag et al., 2017; Schnepf et al., 2015; Koitrand et al., 2015) and would also be the most appropriate boundary condition for the tyres. However, the deformation and contact to the ground do not allow for its use. Additionally, the motion of the lateral

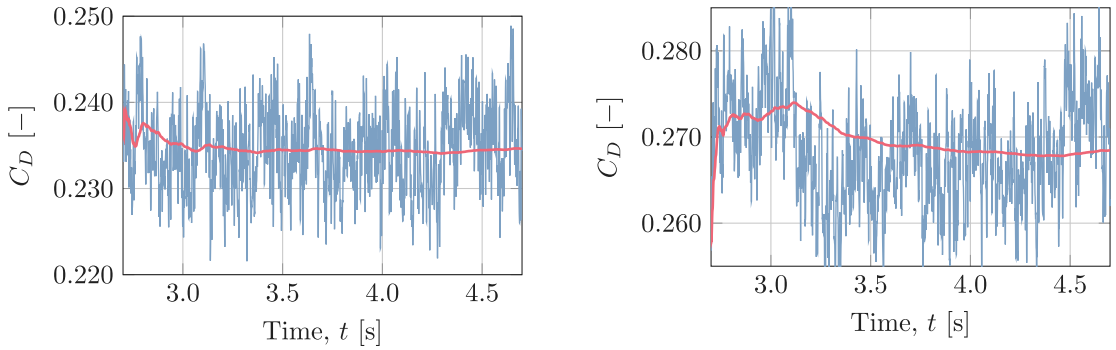

(a) CFD open road (b) CFD PVT

Fig. 11. Instantaneous and running average of C_D in CFD open road and CFD PVT. The averaging is started at $t = 2.7$ s.

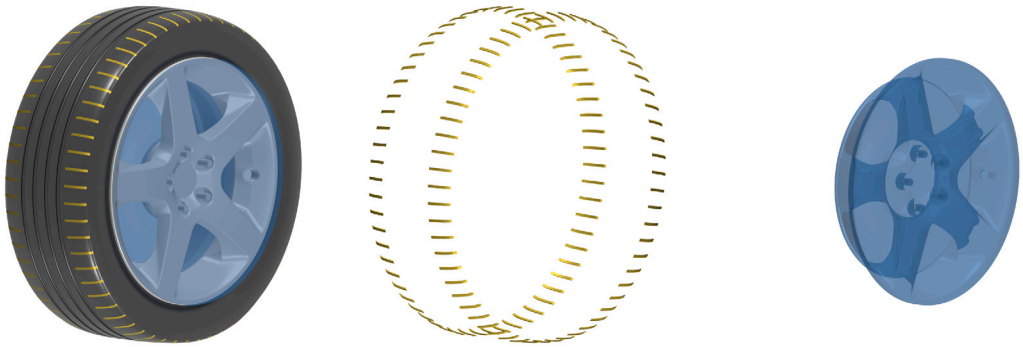

(a) Complete wheel (b) MRFg regions (c) Sliding mesh region (SM)

Fig. 12. Regions and surfaces of the wheel coloured by boundary condition.

grooves cannot be replicated by the rotating wall condition, therefore MRF is used in the grooves. These different regions are shown in Fig. 12.

3. Results

In this section, the findings of this study are presented and reviewed. First, the absolute drag values obtained from experiments and simulations with and without the wind tunnel are introduced. Then, a more detailed analysis focusing on the ability of the numerical procedures to predict the drag differences between configurations of tyres and rims is discussed.

3.1. Absolute drag prediction

In Fig. 13, the drag coefficient is presented for the different tyre and rim combinations. For the experimental data, both the blockage corrected and uncorrected values are shown. The uncorrected data should be compared to the simulations with the wind tunnel geometry (CFD PVT) and the corrected data to the open road simulations (CFD open road). The uncertainty indicated is ±0.001 C_D for the experiments and ±0.002 C_D for the simulations. The experimental uncertainty is based on the in-test repeatability of ±0.001 C_D in the wind tunnel (Ljungskog et al., 2019). The uncertainty in the computations is estimated from the uncertainties observed in the mesh study, time step and averaging time. By including the wind tunnel geometry in CFD the drag prediction is generally improved, reducing the average absolute error between simulations and experiments from 0.005 to 0.002 C_D. CFD open road generally results in an underprediction of drag, indicating that the blockage correction might be too large for this vehicle. The drag for the slick and rain grooved tyres (S and R) with closed rim is significantly underpredicted in CFD open road, suggesting that some flow feature present in the wind tunnel is not replicated in open road.

3.2. Comparison of different tyres

Table 1 and Fig. 14 present the drag difference, ΔC_D, predicted in experiments and the two simulation domains using the corresponding slick tyre configuration as the reference. The uncertainties are propagated from the uncertainties of absolute C_D, resulting in an increase by a factor of $\sqrt{2}$. In general, adding rain grooves reduce the drag whereas the effect of lateral grooves is more dependent on the rim. With the wind tunnel geometry included, ΔC_D is calculated to within the margin of uncertainty for all tyre configurations. For the closed rim, the addition of rain grooves (R) is well predicted even in CFD open road. However, for the tyres with lateral grooves (L and D) the prediction fails in CFD open road. A similar, although slightly less prominent, trend is observed for the open rim.

3.2.1. Influence of tyre pattern with closed rim

In Fig. 15, the accumulated drag difference to the slick tyre is given for the closed rim in CFD open road and CFD PVT. For the rain grooved tyre, a similar trend is observed for both domains. However, for the lateral grooved and the detailed tyres, a discrepancy between the methods can be noted at the rear wheels. The reason for this is illustrated in Fig. 16, where the total pressure coefficient, C_{ptot}, is shown in the plane $z = -300$ mm (17 mm above the ground) at the rear left wheel. As seen, while for the CFD PVT the size and angle of separation are similar for all tyres, these differ with the CFD open road simulations. The larger separation obtained for L and D in CFD

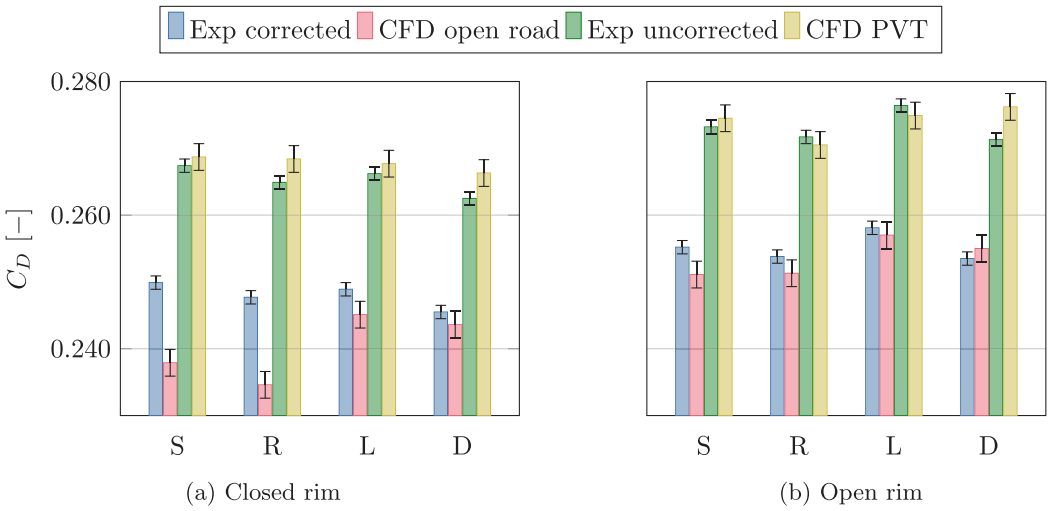

Fig. 13. Drag coefficient, C_D, from physical measurements and numerical simulations with and without the wind tunnel geometry for the four sets of tyres: slicks (S), rain grooves (R), lateral grooves (L) and detailed (D).

Table 1
ΔC_D between the various tyres using the slick tyre as the reference. Data from corrected and uncorrected experiments along with numerical results in both open road and wind tunnel conditions.

Rim	Tyre	Exp corrected	CFD open road	Exp uncorrected	CFD PVT
Closed	S	Ref	Ref	Ref	Ref
	R	−0.002 (−0.9%)	−0.003 (−1.4%)	−0.003 (−0.9%)	0.000 (−0.1%)
	L	−0.001 (−0.4%)	0.007 (+3.0%)	−0.001 (−0.4%)	−0.001 (−0.4%)
	D	−0.004 (−1.8%)	0.006 (+2.4%)	−0.005 (−1.8%)	−0.002 (−0.9%)
Open	S	Ref	Ref	Ref	Ref
	R	−0.001 (−0.5%)	0.000 (+0.1%)	−0.002 (−0.5%)	−0.004 (−1.5%)
	L	0.003 (+1.1%)	0.006 (+2.3%)	0.003 (+1.2%)	0.000 (+0.1%)
	D	−0.002 (−0.7%)	0.004 (+1.6%)	−0.002 (−0.7%)	0.002 (+0.6%)

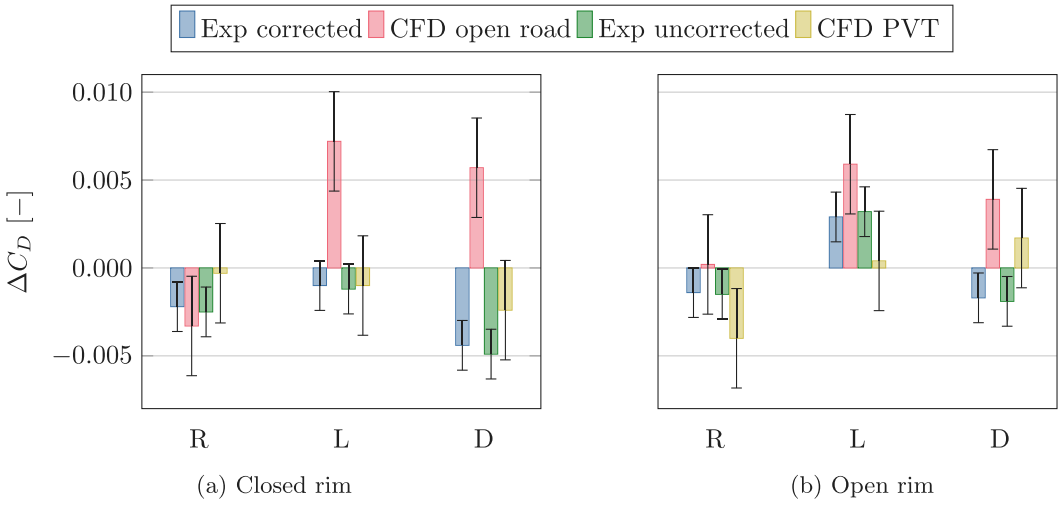

Fig. 14. ΔC_D for the different tyres in the experiments and numerical simulations with and without the wind tunnel geometry. The reference is the slick tyre.

open road, in comparison to the slicks, reduces the acceleration around the inner shoulder, raising the pressure and explaining the increase in accumulated drag at $x = 2.5$ m (Fig. 15). The separation deflects the incoming flow upwards (observed during post-processing, but not shown here), enhancing the pressure in the rear part of the wheelhouse, explaining the additional accumulated drag at $x = 3.1$ m. A clear observation from this figure is the high, respectively, low total pressure coefficient in front of the rear tyre for CFD open road and CFD PVT. This will be explained later in this section.

Differences in rear wheel separation can also be observed in a plane behind the car. In Fig. 17 the total pressure coefficient in the plane $x = 4000$ mm (200 mm behind the bumper) is illustrated for the slick and lateral grooved tyres. Comparing the rear wheel wakes, CFD PVT (Figs. 17(e) and 17(f)) results are in good agreement with the experiments for both tyres. For CFD open road (Figs. 17(c) and 17(d)), contrary to experiments, the tyres have a smaller separation at the ground. Additionally, the fully moving ground simulation in the open road removes the boundary layer growth at the ground on the sides of the car, a condition which is present in the experiments and captured well in CFD PVT. The differences in separation are believed to be caused by how the front wheel wake interacts with the rear wheels. Since a five-belt system is used in PVT, there is no moving

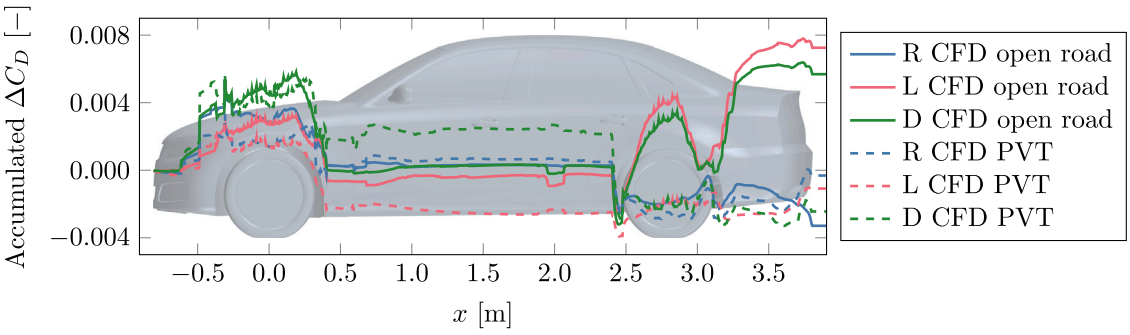

Fig. 15. Accumulated ΔC_D compared to the slick tyre for closed rim.

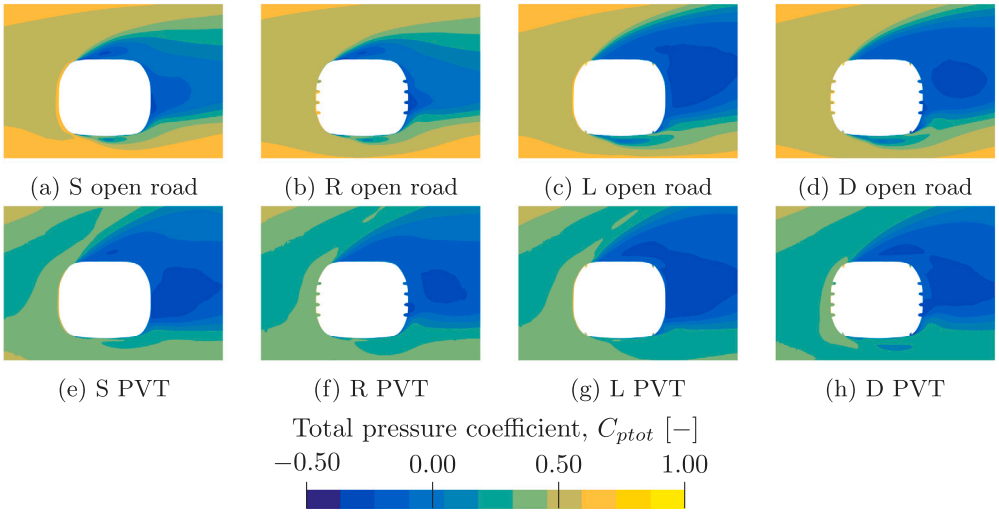

Fig. 16. Total pressure coefficient 17 mm above the ground at the rear left wheel for the closed rim in CFD open road and CFD PVT.

ground between them. The lack of ground simulation results in larger wakes, which to a greater extent shields the rear wheels, see Fig. 18 for the case of slick tyres. This, in turn, causes similar separation for all tyres whereas, in the open road cases, the presence of lateral grooves (L and D) affects the amount and angle of separation. Note that the restraint posts of the wind tunnel do not have an impact on the results as their influence has been investigated, and their effect on the rear tyre separation was shown to be negligible.

3.2.2. Influence of tyre pattern with open rim

Examining the accumulated ΔC_D for the open rim (Fig. 19) similar behaviour as for the closed rim is noted, although, the deltas are somewhat higher, most notably for the detailed tyres. This indicates a greater interaction between the flow around the tyres and the flow through the rim openings. Again, for the open road simulations, the addition of lateral grooves (L and D) increases the separation at the inner shoulder of the rear wheel in comparison to the slicks, Fig. 20. A new observation is that the presence of rain grooves, Figs. 20(b) and 20(d), results in a somewhat smaller separation compared to the tyres without them, Figs. 20(a) and 20(c). For CFD PVT, the rear wheels are well protected by the front wheel wakes, therefore, differences among tyres are less visible. However, a reduction in wake size with the addition of rain grooves is apparent.

3.3. Comparison of different rims

In Section 3.2 the differences in drag and flow field from varying the tread pattern with and without the wind tunnel geometry were discussed. Here, the effect of including the wind tunnel in CFD on the ability to predict variations between rims for a specific tyre pattern is investigated. The results are presented in Table 2 and Fig. 21, with ΔC_D calculated using the corresponding closed rim configuration as the reference. In general, the inclusion of the wind tunnel geometry improves the prediction in CFD, in particular for the slick and rain grooved tyres. For the lateral grooved and detailed tyres, ΔC_D is predicted to within the uncertainty for both domains.

Table 2
Absolute and relative ΔC_D between the closed and open rim in experiments and CFD.

Tyre	Exp corrected	CFD open road	Exp uncorrected	CFD PVT
S	0.005 (+2.1%)	0.013 (+5.5%)	0.006 (+2.2%)	0.006 (+2.2%)
R	0.006 (+2.5%)	0.017 (+7.1%)	0.007 (+2.6%)	0.002 (+0.8%)
L	0.009 (+3.7%)	0.012 (+4.9%)	0.010 (+3.8%)	0.007 (+2.7%)
D	0.008 (+3.3%)	0.011 (+4.7%)	0.009 (+3.4%)	0.010 (+3.7%)

The accumulated ΔC_D (Fig. 22) shows that, at the front wheels, the difference between closed and open rims is comparable in both domains for the lateral grooved tyre. For the slick tyre, the influence of the front wheel rim is more dependent on the domain. A similar trend for the addition of lateral grooves is also observed when comparing the rain grooved and detailed tyres (not shown here). This is explained by the skin friction coefficient, C_f, plotted in Fig. 23. For the slick tyre, C_f indicates similar flow fields for the closed rim in both domains (Figs. 23(a) and 23(b)). However, for the open rim a more attached flow is obtained in CFD open road (Fig. 23(c)) compared to CFD PVT (Fig. 23(d)), most notable at the upper front of the outer tyre shoulder. This clarifies the variation in accumulated ΔC_D at the front wheel. For the lateral grooved tyre, the skin friction coefficient indicates that

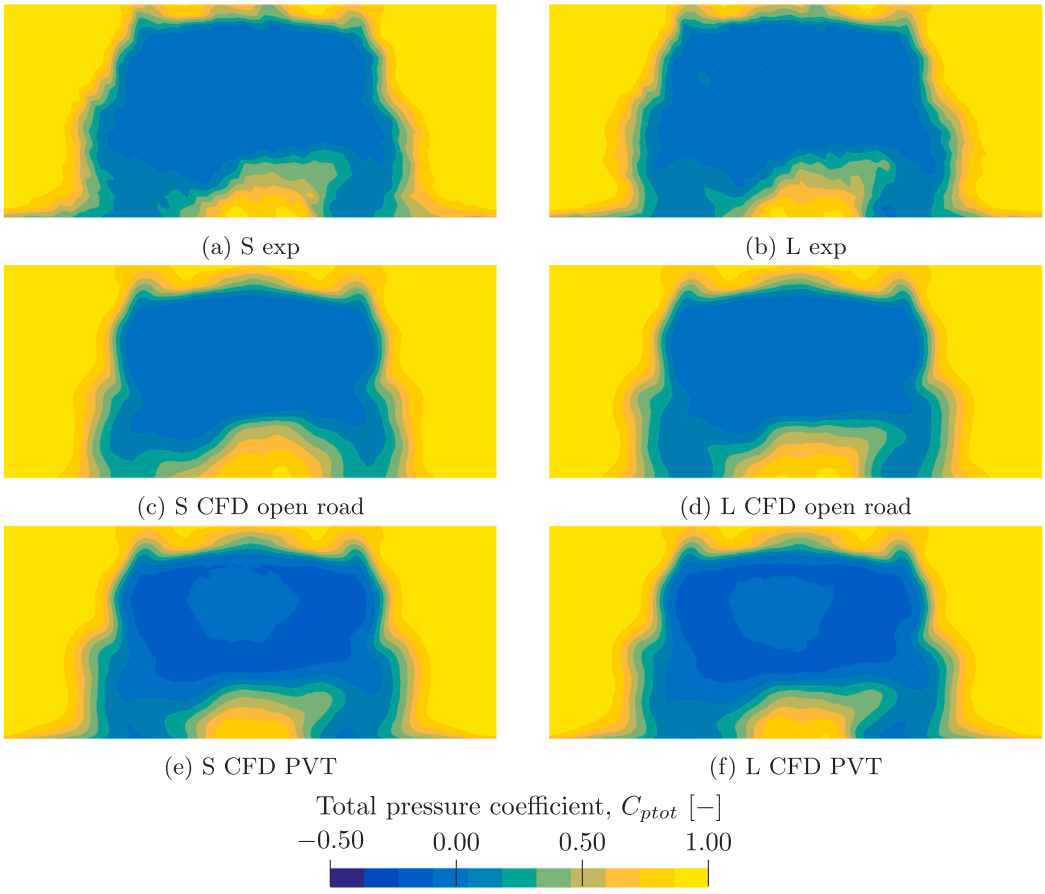

Fig. 17. Total pressure coefficient for the slick (S) and lateral grooved (L) tyres with closed rim in the plane $x = 4000$ mm. Experimental results and results from CFD open road and CFD PVT.

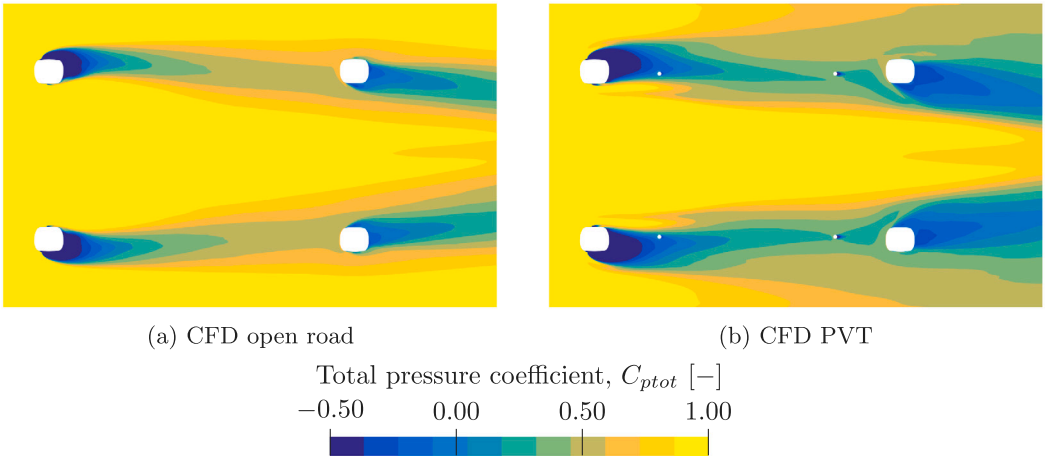

Fig. 18. Total pressure coefficient 17 mm above the ground for the slick tyre with closed rim in CFD open road and CFD PVT.

the flow fields are similar for both rims in both domains (Figs. 23(e)–23(h)). The differences observed for the slick tyre is believed to be caused by the blockage of the wind tunnel walls, rather than by the differences in ground simulation. As described by Ljungskog et al. (2019), the inclusion of the wind tunnel geometry changes the flow around the vehicle and alters the sensitivity to separation, especially in areas of high acceleration, such as at the corner of the front bumper and the tyre shoulder. For a tyre with a smooth shoulder (S and R), the separation would be largely determined by the rim, whereas for a tyre with lateral grooves (L and D) the separation would, to a greater extent, be determined by both the tyre and rim.

Further downstream, much of the differences between CFD open road and CFD PVT are due to changes in the base pressure. For CFD open road, open rims increase the drag at the base with at least 0.005 C_D for all tyres, while for CFD PVT only small variations are observed (Fig. 22). The base pressure coefficient deltas, calculated as $\Delta C_p = C_{p,\mathrm{OR}} - C_{p,\mathrm{CR}}$, are illustrated for the slick tyre in Fig. 24. As for the front wheels, it is believed that the differences between the methods can be explained by the blockage. Fig. 25 presents the total pressure

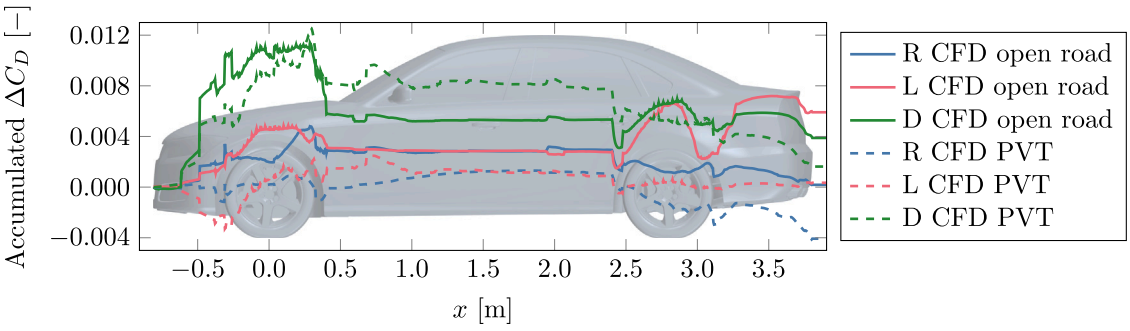

Fig. 19. Accumulated ΔC_D compared to the slick tyre for open rim.

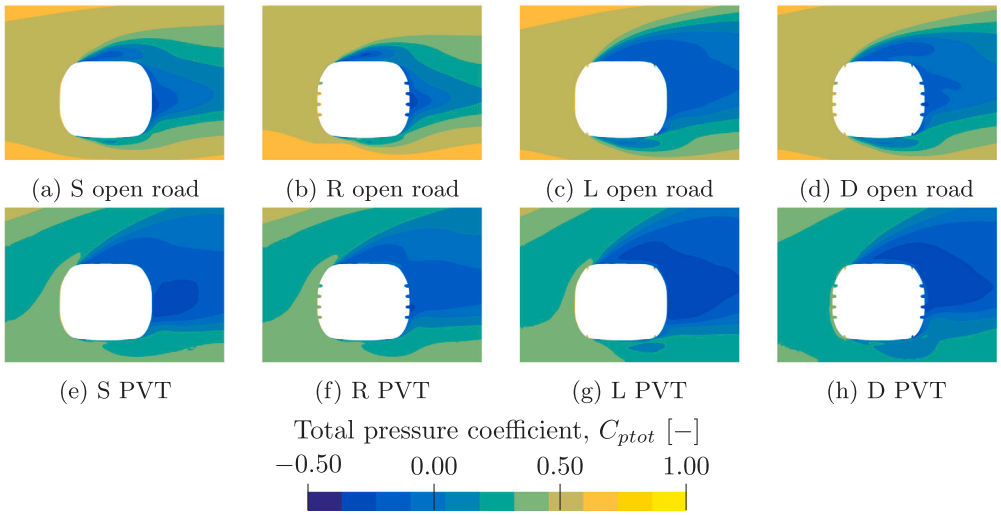

Fig. 20. Total pressure coefficient 17 mm above the ground at the rear left wheel for the open rim in CFD open road and CFD PVT.

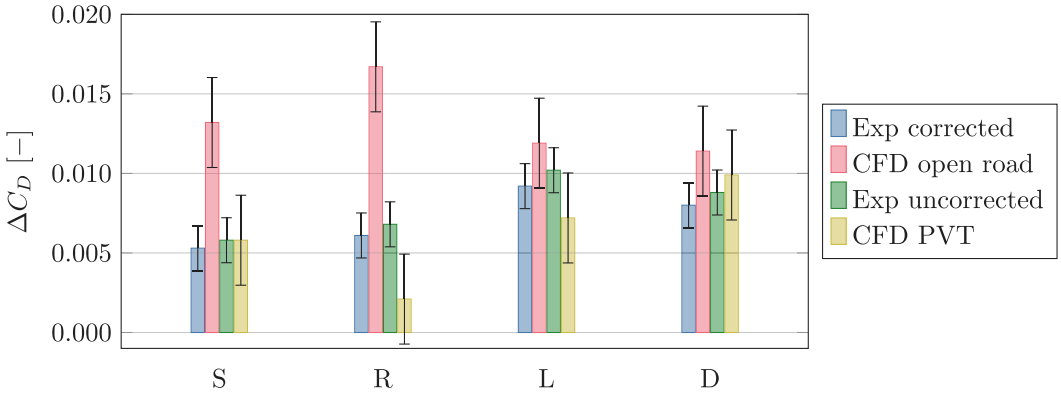

Fig. 21. ΔC_D between the closed and open rim for different tyres in CFD open road and CFD PVT compared to experiments.

coefficient in the plane $x = 4000$ mm for the slick tyre with closed and open rims. Looking at the separation from the outer surfaces of the rear wheels at approximately the wheel centre height, the width does not change much when comparing closed and open rims in the wind tunnel, whereas a widening is observed when changing from closed to open rims in open road conditions.

3.4. Summary of results

To summarise the findings, we define the delta of deltas as

$$\Delta\Delta C_{D,\mathrm{x}} = \left(C_{D,\mathrm{x}} - C_{D,\text{S-CR}}\right)_{\mathrm{CFD}} - \left(C_{D,\mathrm{x}} - C_{D,\text{S-CR}}\right)_{\mathrm{exp}}, \quad (6)$$

where the index x denotes the configuration in consideration and S-CR means that the slick tyre with closed rim is the reference. In Eq. (6), deltas in CFD open road are compared to corrected experimental deltas, while CFD PVT is compared to uncorrected experimental values. These are presented in Fig. 26. The uncertainty of 0.003 $\Delta\Delta C_D$ is propagated from the uncertainties of absolute C_D. From the results it can be seen that the inclusion of the wind tunnel geometry leads to more accurate and consistent predictions. It should be noted that because of the large deviation between the simulations in the two domains for the slick tyre with closed rim, Fig. 13, having this configuration as the reference exaggerates the differences somewhat. Nevertheless, it is clear that

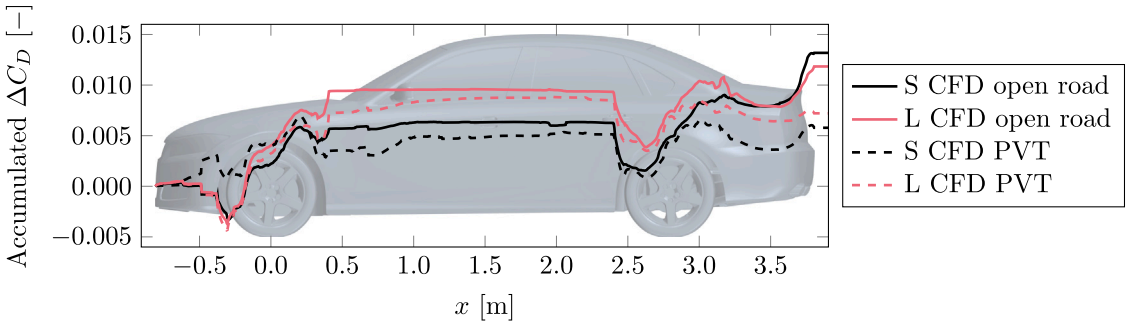

Fig. 22. Accumulated ΔC_D between open and closed rims for the slick (S) and lateral grooved (L) tyres.

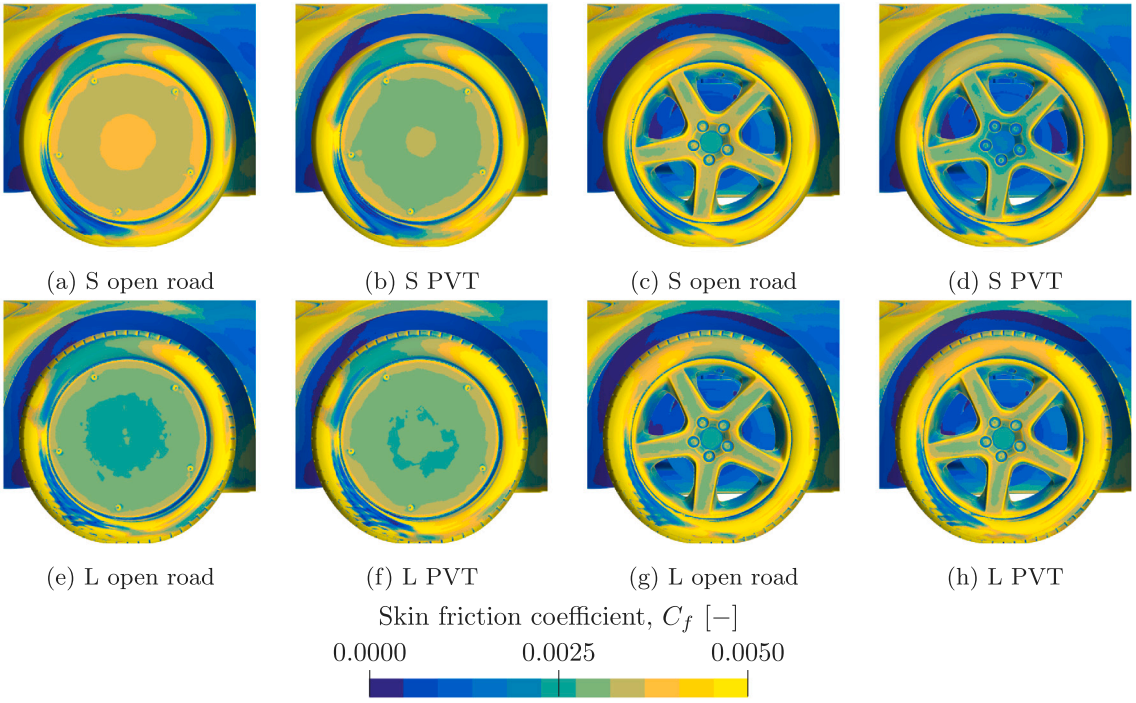

Fig. 23. Skin friction coefficient at the front left wheel for slick (S) and lateral grooved (L) tyres in CFD open road and CFD PVT.

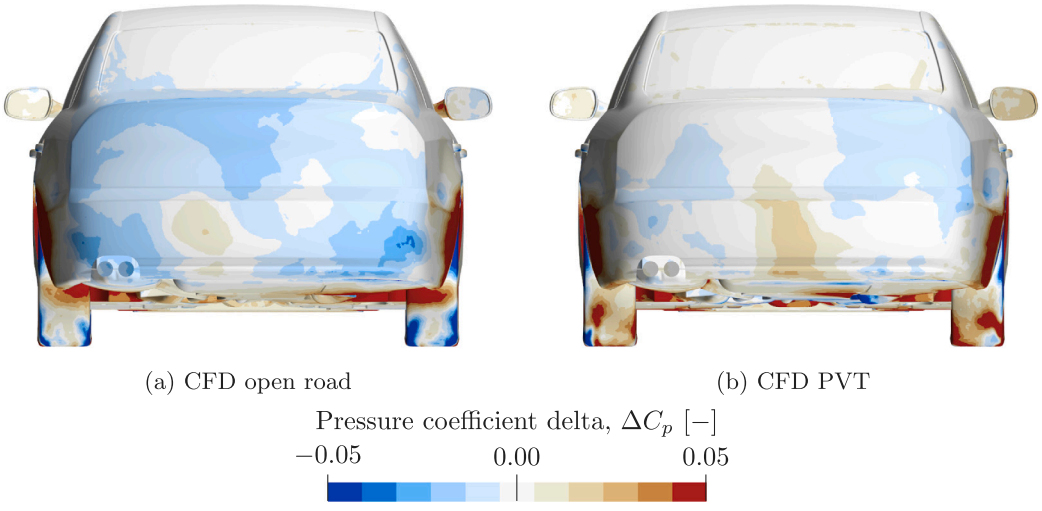

Fig. 24. Difference in pressure coefficient between open and closed rims for the slick tyre. A positive value indicates that the pressure is higher with the open rim.

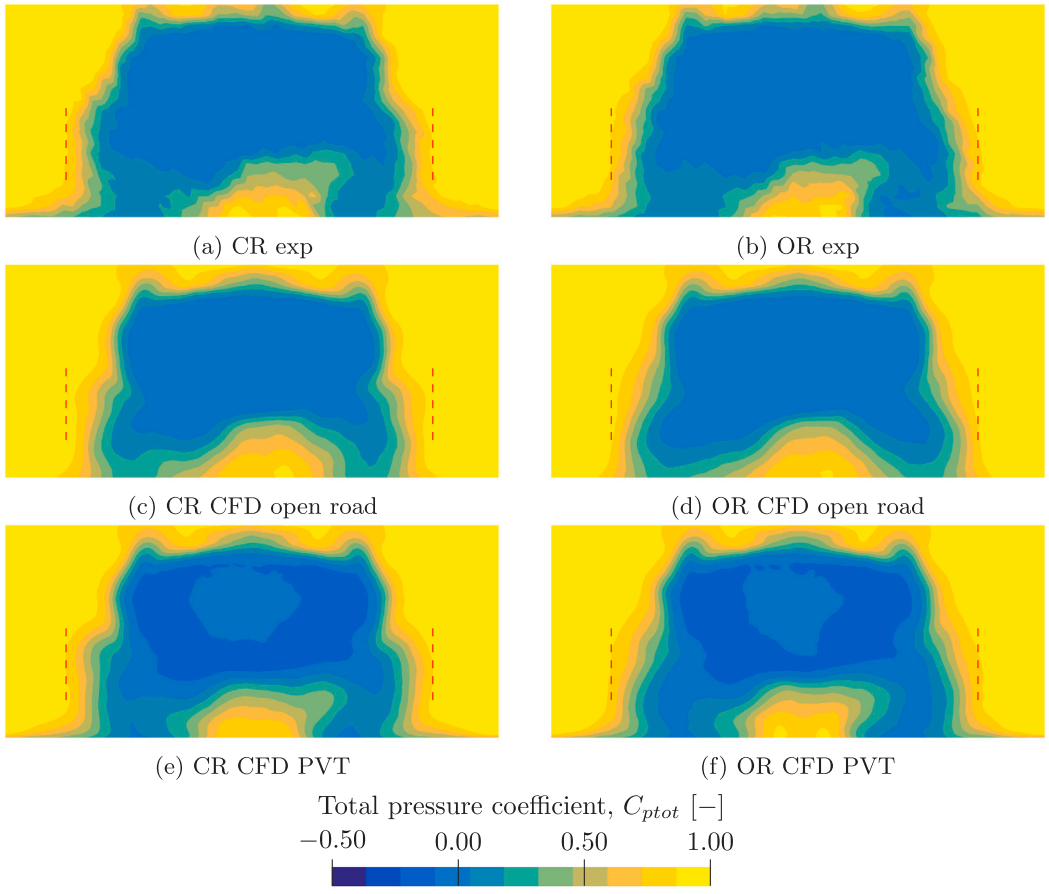

Fig. 25. Total pressure coefficient in the plane $x = 4000\,\text{mm}$ for the slick tyre with open and closed rims. The lines have been added to assist assessing the width of the separation and are placed at the same location for all cases.

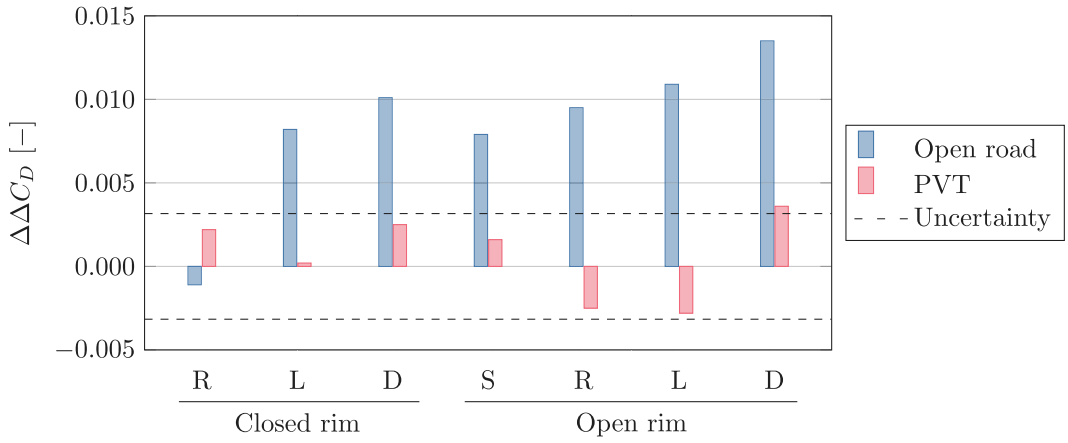

Fig. 26. $\Delta\Delta C_D$ showing the difference between open road (CFD open road and corrected experimental data) and PVT (CFD PVT and uncorrected experimental data) conditions. The baseline configuration is the slick tyre with closed rim.

a better prediction is obtained when the wind tunnel geometry is included in the simulations.

4. Conclusions

The effect of including the wind tunnel geometry in numerical simulations, as compared to replicating open road conditions, on the prediction of wheel aerodynamics has been investigated in this paper. The results of the simulations were compared with measurements from the wind tunnel using both uncorrected and blockage corrected values. For most cases, the inclusion of the wind tunnel in CFD improved the prediction of the absolute drag coefficients as well as the prediction of drag deltas between wheel configurations. Comparing tyre patterns, rain grooves generally decreased drag while the effect of lateral grooves was more dependent on the type of rim and simulation domain. The wind tunnel simulations were able to replicate the differences in drag to within the margin of uncertainty, whereas open road simulations were less consistent, especially for the tyres with lateral grooves on a closed rim. Regarding open and closed rims, it was found that open road simulations predicted larger drag changes than simulations with

the wind tunnel geometry, most notably for the slick and rain grooved tyres, with an overestimation by a factor of three.

Summarising, the largest discrepancies between the two simulation setups are observed among tyres with lateral grooves and among open rims with slick and rain grooved tyres. The tunnel walls and the ground simulation system have an impact on the predicted flow fields and forces. The blockage alters the separations at the tyre shoulder and outer rim surface, whereas the ground simulation system affects the interaction between the front wheel wakes and the rear wheels.

CRediT authorship contribution statement

Erik Josefsson: Conceptualization, Methodology, Software, Validation, Formal analysis, Investigation, Data curation, Writing – original draft, Visualization. **Teddy Hobeika:** Conceptualization, Methodology, Resources, Writing – review & editing, Supervision, Project administration, Funding acquisition. **Simone Sebben:** Conceptualization, Methodology, Resources, Writing – review & editing, Supervision, Funding acquisition.

Declaration of competing interest

The authors declare that they have no known competing financial interests or personal relationships that could have appeared to influence the work reported in this paper.

Acknowledgements

The authors would like to thank Ford of Europe, particularly Dr. Burkhard Hupertz and Manfred Lentzen, for the collaboration, making the DrivAer available and sharing their expertise regarding the model. This work is funded by the Swedish Energy Agency P49114-1 and Volvo Cars, Sweden. The computations were enabled by resources provided by the Swedish National Infrastructure for Computing (SNIC) at Tetralith partially funded by the Swedish Research Council through grant agreement no. 2018-05973.

References

Aeroprobe corporation, 2015. Standard probes user manual.

Ashton, N., Skaperdas, V., Sinclair, O., Van Noordt, W., 2019. First Automotive CFD Prediction Workshop, Cross-Plotting - Case2a/b. Oxford, [Online]. Available: https://autocfd1.s3.eu-west-1.amazonaws.com/Presentations/Case2-summary-v2.pdf.

Avadiar, T., Thompson, M.C., Sheridan, J., Burton, D., 2018. Characterisation of the wake of the DrivAer estate vehicle. J. Wind Eng. Ind. Aerodyn. 177, 242–259.

Cogotti, A., 1983. Aerodynamic characteristics of car wheels. Int. J. Veh. Des..

Croner, E., Bézard, H., Sicot, C., Mothay, G., 2013. Aerodynamic characterization of the wake of an isolated rolling wheel. Int. J. Heat Fluid Flow 43, 233–243.

Cyr, S., Ih, K.-D., Park, S.-H., 2011. Accurate Reproduction of Wind-Tunnel Results with CFD. SAE Technical Paper 2011-01-0158.

Davidson, L., 2009. Large Eddy simulations: How to evaluate resolution. Int. J. Heat Fluid Flow 30 (5), 1016–1025.

Diasinos, S., Barber, T.J., Doig, G., 2015. The effects of simplifications on isolated wheel aerodynamics. J. Wind Eng. Ind. Aerodyn. 146, 90–101.

Ekman, P., Larsson, T., Virdung, T., Karlsson, M., 2019. Accuracy and Speed for Scale-Resolving Simulations of the DrivAer Reference Model. SAE Technical Paper 2019-01-0639.

Ekman, P., Wieser, D., Virdung, T., Karlsson, M., 2020. Assessment of hybrid RANS-LES methods for accurate automotive aerodynamic simulations. J. Wind Eng. Ind. Aerodyn. 206.

Eng, M., Walker, T., 2009. Investigation of aerodynamic correction methods applied to a slotted wall wind tunnel. In: Proceedings of Euromech Colloquium 509. Berlin, pp. 59–69, https://depositonce.tu-berlin.de/handle/11303/2466.

Fischer, O., Kuthada, T., Mercker, E., Wiedemann, J., Duncan, B., 2010. CFD Approach to Evaluate Wind-Tunnel and Model Setup Effects on Aerodynamic Drag and Lift for Detailed Vehicles. SAE Technical Paper 2010-01-0760.

Fischer, O., Kuthada, T., Wiedemann, J., Dethioux, P., Mann, R., Duncan, B., 2008. CFD Validation Study for a Sedan Scale Model in an Open Jet Wind Tunnel. SAE Technical Paper 2008-01-0325.

Haag, L., Kiewat, M., Indinger, T., Blacha, T., 2017. Numerical and experimental investigations of rotating wheel aerodynamics on the drivaer model with engine Bay flow. In: ASME 2017 Fluids Engineering Division Summer Meeting.

Heft, A.I., Indinger, T., Adams, N.A., 2012. Introduction of a New Realistic Generic Car Model for Aerodynamic Investigations. SAE Technical Paper 2012-01-0168.

Hobeika, T., Sebben, S., 2018a. Tyre pattern features and their effects on passenger vehicle drag. SAE Int. J. Passeng. Cars Mech. Syst. 11 (5), 401–413.

Hobeika, T., Sebben, S., 2018b. CFD investigation on wheel rotation modelling. J. Wind Eng. Ind. Aerodyn. 174, 241–251.

Hucho, W.-H., 1998. Aerodynamics of Road Vehicles, fourth ed. SAE International, Warrendale.

Hupertz, B., Chalupa, K., Krueger, L., Howard, K., Glueck, H.-D., Lewington, N., Chang, J.-H., Shin, Y.-s., 2021. On the Aerodynamics of the Notchback Open Cooling DrivAer: A Detailed Investigation of Wind Tunnel Data for Improved Correlation and Reference. SAE Technical Paper 2021-01-0958.

Hupertz, B., Krüger, L., Chalupa, K., Lewington, N., Luneman, B., Costa, P., Kuthada, T., Collin, C., 2018. Introduction of a new full-scale open cooling version of the DrivAer generic car model. In: Progress in Vehicle Aerodynamics and Thermal Management. Springer International Publishing, Cham, pp. 35–60.

Koitrand, S., Gaylard, A., Fiet, G.O., 2015. An investigation of wheel aerodynamic effects for a saloon car. In: Proceedings of the 10th FKFS-Conference. pp. 240–255.

Ljungskog, E., Sebben, S., Broniewicz, A., 2019. Inclusion of the physical wind tunnel in vehicle CFD simulations for improved prediction quality. J. Wind Eng. Ind. Aerodyn. 197.

Mayer, W., Wiedemann, J., 2007. The Influence of Rotating Wheels on Total Road Load. SAE Technical Paper 2007-01-1047.

Reiß, J., Sebald, J., Haag, L., Zander, V., Indinger, T., 2020. Experimental and Numerical Investigations on Isolated, Treaded and Rotating Car Wheels. SAE Technical Paper 2020-01-0686.

Schnepf, B., Schütz, T., Indinger, T., 2015. Further investigations on the flow around a rotating, isolated wheel with detailed tread pattern. SAE Int. J. Passeng. Cars Mech. Syst. 8 (1), 261–274.

Siemens, 2021. External Aerodynamics with Simcenter STAR-CCM+ Best Practice Guidelines (2021.3). Tech. Rep., [Online]. Availbale: https://support.sw.siemens.com/knowledge-base/KB000041270_EN_US.

Sternéus, J., Walker, T., Bender, T., 2007. Upgrade of the Volvo Cars Aerodynamic Wind Tunnel. SAE Technical Paper 2007-01-1043.

Strangfeld, C., Wieser, D., Schmidt, H.-J., Woszidlo, R., Nayeri, C., Paschereit, C., 2013. Experimental Study of Baseline Flow Characteristics for the Realistic Car Model Drivaer. SAE Technical Paper 2013-01-1251.

Wang, S., Avadiar, T., Thompson, M.C., Burton, D., 2019. Effect of moving ground on the aerodynamics of a generic automotive model: The DrivAer-Estate. J. Wind Eng. Ind. Aerodyn. 195.

Wang, Y., Sicot, C., Borée, J., Grandemange, M., 2020. Experimental study of wheel-vehicle aerodynamic interactions. J. Wind Eng. Ind. Aerodyn. 198.

Wäschle, A., 2007. The Influence of Rotating Wheels on Vehicle Aerodynamics - Numerical and Experimental Investigations. SAE Technical Paper 2007-01-0107.

Wickern, G., Zwicker, K., Pfadenhauer, M., 1997. Rotating wheels - Their mpact on wind tunnel test techniques and on vehicle drag results. SAE Trans. 254–270.

Wittmeier, F., Kuthada, T., 2015. Open grille drivaer model - First results. SAE Int. J. Passeng. Cars Mech. Syst. 8 (2015-01-1553), 252–260.

Wittmeier, F., Kuthada, T., Widdecke, N., Wiedemann, J., 2014. Model Scale Based Process for the Development of Aerodynamic Tire Characteristics. SAE Technical Paper 2014-01-0585.